CHEMISTRY OF MATERIALS

pubs.acs.org/cm

Article

Pressure-Induced Conglomerate to Racemate Transformation in a One-Dimensional Disulfide-Based Lead Halide

Wenbo Qiu, Weilong He, Yu Liu, Boyang Fu, Weiyi Wang, Jiangang He, Luhong Wang, Haozhe Liu, and Weizhao Cai*

Cite This: *Chem. Mater.* 2025, 37, 2953−2963

Read Online

ACCESS | Metrics & More | Article Recommendations | Supporting Information

ABSTRACT: Controlling the molecular chirality under external pressure is particularly challenging in low-dimensional hybrid halides, as the constrained structure and strong hydrogen bonding hinder significant conformational changes in bulky organic molecules. Here, by incorporating flexible disulfide-based molecules into the one-dimensional (1D) PbI_5 framework, the chiral hybrid halide $[NH_3(CH_2)_2S{-}S(CH_2)_2NH_3]PbI_5{\cdot}H_3O$ undergoes a transformation from conglomerate to racemate at a hydrostatic pressure of approximately 0.10 GPa. This reversible acentric-to-centric transformation is accompanied by the second-harmonic generation (SHG) "on−off" switching and significant conformational changes in the cystamine cations within the structure. In the high-pressure racemic phase, two enantiomers with left- and right-handed conformers (M- and P-helicity) coexist within the lattice structure and their deformations under compression resemble those of a compressed mechanical spring, ultimately leading to considerable distortions of the 1D zigzag PbI_5 chains through strong organic−inorganic H···I interactions. Furthermore, both experimental and theoretical results reveal that the unique phase transformation induces minor alterations in the electronic structures and optical bandgaps. Our findings provide insights into the manipulation of molecular chirality and SHG properties in hybrid halides by introducing flexible organic molecules into inorganic frameworks.

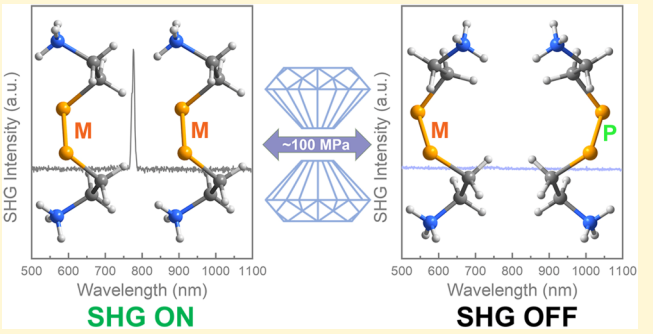

INTRODUCTION

The molecular chirality conversion under external stimuli presents a significant challenge for the synthesis and production of chiral compounds, particularly in the pharmaceutical and food industries.[1] In solid crystalline materials, racemates are defined by the coexistence of both enantiomers within the crystal lattice in equal proportions. The mechanical mixture of crystals containing the two pure enantiomers is termed a conglomerate, which represents the case of spontaneous resolution.[2] Previous studies on soft matter, such as liquid crystals and coordination polymers, have demonstrated that the chiral inversions can be induced by external stimuli, e.g., chemical solvents,[3−5] light,[6,7] and strain.[8] However, molecular chirality switching (or conglomerate-racemate transformation) remains more challenging to achieve in the solid crystalline phase due to the presence of a restricted structure and strong hydrogen bonding, which impedes large conformational changes even under extremely high pressure. For example, DL-mandelic acid exhibits a lower density than its D and L enantiomers, retaining its racemic structure and undergoing a phase transition at 0.65 GPa. Its crystal structure becomes more compacted under compression, suggesting that it is unlikely to resolve into enantiomers, even at pressures as high as 2.6 GPa.[9,10] The hexagonal L-cystine, which contains highly flexible molecules, features right-handed helices connected by disulfide bridges. Its ambient-pressure $P6_122$ structure remains stable over a wide pressure range (0−25 GPa) owing to strong interlayer NH···O hydrogen bonds.[11,12] The strong preference for either the racemate or the conglomerate under compression can be attributed to the substantial internal energy contributions to the Gibbs free energy from the strong directional hydrogen bonds and the conformational energy of organic molecules, which are considerably larger than the work contributed by external pressure.[13−15] Therefore, pressure-induced transformations that resolve the racemate into the conglomerate, or vice versa, are rarely reported.

When a perovskite material incorporates chiral organic molecules (e.g., phenylethylamine) into the inorganic framework, it typically forms low-dimensional chiral structures with interesting physical properties, including ferroelectricity,[16,17]

Received: February 10, 2025
Revised: March 23, 2025
Accepted: March 24, 2025
Published: March 28, 2025

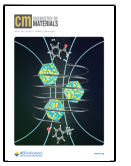

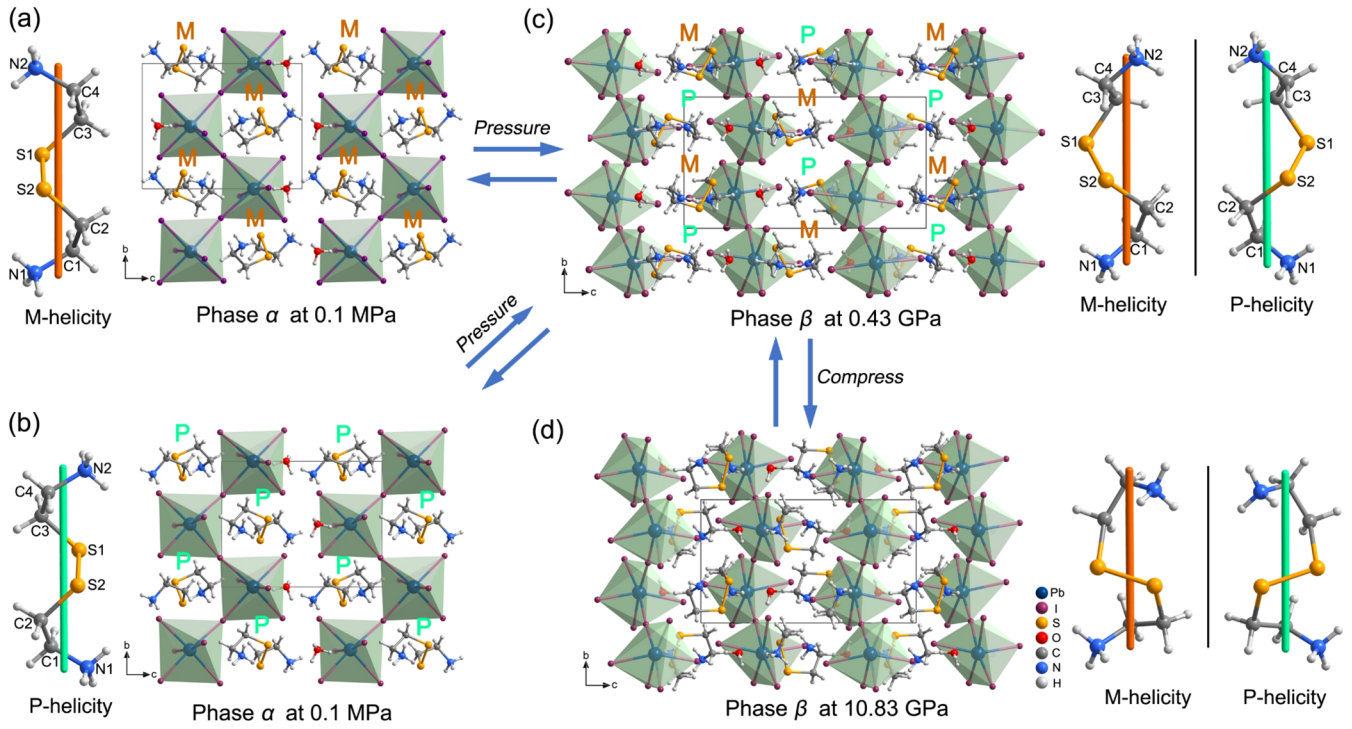

Figure 1. Crystal structures of **1** viewed along the [100] direction. (a, b) Phase α at 0.1 MPa (M- and P-helicity). (c) Phase β at 0.43 GPa. (d) Phase β at 10.83 GPa. The conformational changes of the organic cations $[NH_3(CH_2)S{-}S(CH_2)_2NH_3]^{2+}$ during the phase α-β phase transition are shown for comparison.

nonlinear optics,[18,19] and circularly polarized luminescence.[20,21] When subjected to external pressure, these halides typically undergo significant distortions of the inorganic framework due to the elevated steric hindrance of the bulky organic cations under compression.[22−25] In contrast to the robust organic cations, acyclic disulfides R−SS−R′ (where R and R′ are nonchiral organic groups) adopt a screw-like geometry in the crystalline state, with two enantiomeric conformers exhibiting chiral M- and P-helical configurations. The ideal C−S−S−C torsion angle is 90°, and the energy barrier for interconversion between the two conformers is relatively low (ca. 6 kcal mol^{-1}).[26] In the hybrid halide system, incorporating flexible disulfide-based organic cations into the inorganic framework generally results in the formation of enantiomorphous systems,[27] which leads to intriguing nonlinear optical properties.[28,29] Previous studies on cystamine-based perovskites have demonstrated that the molecular chirality can be switched by external stimuli, such as temperature[30] and electric field.[31] Pressure has been shown to be an effective approach of modulating lattice distortions, unique organic molecular arrangements, as well as the electronic properties in hybrid halides.[32−36] However, investigations into the effects of external pressure on hybrid halides incorporating A-site chiral disulfide-based molecules have not yet been explored.

In this work, we synthesized the one-dimensional (1D) lead halide $[NH_3(CH_2)_2S{-}S(CH_2)_2NH_3]PbI_5{\cdot}H_3O$ (**1**), which exhibits a perovskite-like structure. In this compound, the diprotonated cystamine molecules exist as helical conformers in M or P forms, which are incorporated into the corner-sharing PbI_6 octahedra inorganic framework. By employing high-pressure single-crystal X-ray diffraction, we observed a pressure-induced reversible acentric-to-centric transformation, accompanied by the disappearance of second-harmonic generation (SHG) signal. Remarkably, the M or P conformers in the ambient pressure phase transform into a high-pressure racemic phase, where both M and P conformers coexist within the lattice. As the pressure increases, the strong organic−inorganic interactions induce considerable distortions of the 1D zigzag PbI_5 chain and significant conformational changes in the helical organic cations. The transformation also leads to a slight reduction in the energy bandgap, as demonstrated by the UV−vis absorption measurements. Furthermore, variations in the electronic structures of phases α and β were investigated by the density functional theory (DFT) calculations, which demonstrated that the constituents of the density of states near the Fermi level are primarily contributed by the inorganic octahedral framework in both phases.

RESULTS AND DISCUSSION

Light yellow, needle-shaped single crystals of **1** were synthesized via the solvothermal method at 353 K in a Teflon autoclave using PbI_2, cystamine dihydrochloride and concentrated HI in acetonitrile, as described previously.[30] At ambient conditions, compound **1** crystallizes in the polar monoclinic space group $P2_1$, with lattice parameters a = 10.4199(17) Å, b = 8.8820(19) Å, c = 11.701(3) Å and β = 104.458(7)° (Z = 2, denoted as phase α, M-helicity, left-handed helical form, crystal A). Variable temperature single-crystal X-ray diffraction (SXRD) measurements at ambient pressure reveal that phase α is stabilized upon cooling the sample to 100 K (see Table S1). However, upon warming to 348 K, phase α transforms into the centrosymmetric phase β (space group $P2_1/n$) with disordered cystamine molecules.[30] Interestingly, the β phase is denser than the ambient pressure phase α at room temperature, which contradicts the general rule. Furthermore, randomly selected single crystals characterized by SXRD exhibit either P- or M-helicity in the organic

https://doi.org/10.1021/acs.chemmater.5c00335
Chem. Mater. 2025, 37, 2953−2963

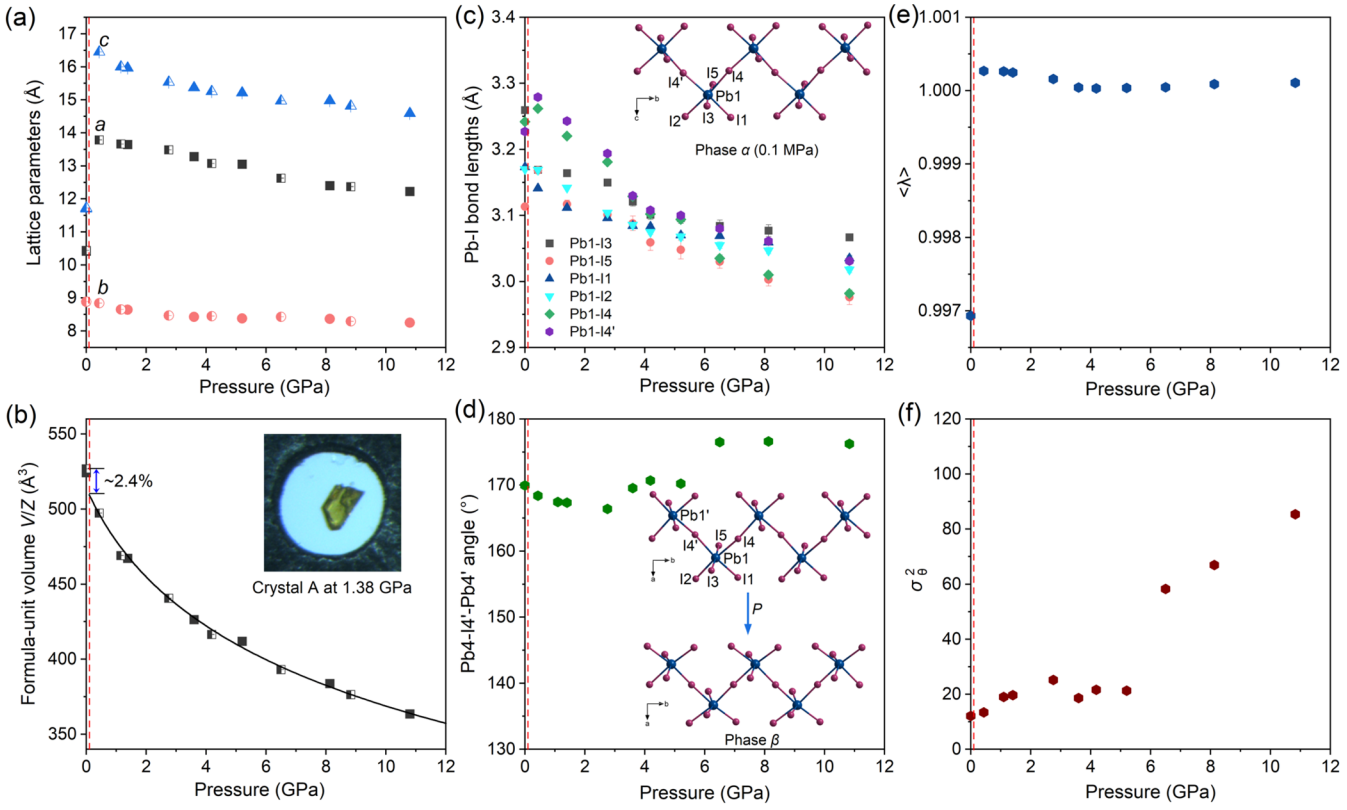

Figure 2. Lattice parameters and structural parameters of compound **1** under pressure. (a, b) Lattice parameter *a*, *b*, *c* and formula-unit volume (*V*/*Z*) as a function of pressure. The inset shows the optical image of single crystal A compressed in the DAC chamber for SXRD measurements. The full and half-filled symbols indicate the data from single crystals A and B, respectively. (c, d) Changes of Pb−I bond lengths as a function of pressure. The 1D zigzag PbI_5 chain in phases α and β under compression are shown in the inset. (e, f) Evolution of average quadratic elongation ($<\lambda>$) and average bond angle variance (σ_θ^2) under compression. The dashed lines in all the panels indicate the phase α-β transition at ∼0.1 GPa.

cations $[NH_3(CH_2)_2S{-}S(CH_2)_2NH_3]^{2+}$, thereby confirming the presence of only one enantiomeric form of cystamine in the structure of phase α. Hence, compound **1** exists as a conglomerate at ambient conditions (P-helicity, right-handed helical form, crystal B, see Table S1). The crystal structure of phase α consists of 1D zigzag chains of corner-sharing PbI_6 octahedra extending along the [010] direction and separated by the skewed cystamine cations $[NH_3(CH_2)_2S{-}S{-}(CH_2)_2NH_3]^{2+}$ and H_3O^+ hydronium cations (Figure 1a,b). As with other reported lead iodide perovskites, the Pb−I bond lengths range from 3.1132(13) to 3.2595(13) Å, consistent with previous reports.[37,38] The cystamine cations exhibit a screw-like structure, with the C(2)−S(2)−S(1)−C(3) torsion angle of −85.1(9)° for M-helicity and −85.4(4)° for P-helicity, respectively. The $-NH_3$ groups located at the head and tail of organic cations interact with the neighboring 1D PbI_5 chains through NH···I hydrogen bonds (ranging from 2.686 to 2.982 Å at 0.1 MPa/296 K), whereas no strong intermolecular interactions are observed around the C and S atoms (Figure S1a). The hydronium cation H_3O^+, with its hydrogen atoms treated as riding models also interacts with the inorganic PbI_5 network, exhibiting the shortest OH···I distance of 2.656 Å (O···I distances range from 3.530 to 3.700 Å).

We have determined the crystal structures of compound **1** up to 10.83 GPa by means of single-crystal X-ray diffraction at room temperature. With increasing the pressure, phase α stabilizes within a narrow pressure range at room temperature and transforms into the β phase as the pressure reaches 0.15 GPa. High-pressure SXRD measurements on both crystals A and B revealed that the β phase is centrosymmetric, with the monoclinic space group $P2_1/n$ (crystal B at 0.43 GPa, $Z = 4$, $a = 13.7859(17)$ Å, $b = 8.8435(7)$ Å, $c = 16.4488(16)$ Å, and $\beta = 97.225(8)°$, Table S2). The packing arrangements of the inorganic framework in the β phase are similar to those in phase α, with significant changes occurring in the organic molecules. Phase β adopts the same structure as the high temperature phase, but with the organic molecules ordered (Figure 1c,d).[30] The emergence of the inversion center in the structure of phase β implies that both M and P cystamine conformers coexist, making phase β as a racemic compound. To the best of our knowledge, such uncommon phenomenon of a conglomerate converting to a racemate under external pressure represents an extremely rare example in 1D hybrid halides.[31] The unit-cell relationship between phases α and β can be expressed by the following matrix equation

$$\begin{pmatrix} \boldsymbol{a}_\beta \\ \boldsymbol{b}_\beta \\ \boldsymbol{c}_\beta \end{pmatrix} = \begin{pmatrix} 1 & 0 & 1 \\ 0 & -1 & 0 \\ 1 & 0 & -1 \end{pmatrix} \begin{pmatrix} \boldsymbol{a}_\alpha \\ \boldsymbol{b}_\alpha \\ \boldsymbol{c}_\alpha \end{pmatrix}$$

During the phase transition, the lattice parameter *b* remains continuous, whereas the lattice parameters *a* and *c* expand largely and angle β undergoes a sudden reduction of ∼7.2° (Figures 2 and S2). The changes in symmetry element from phase α to β reveal that the transformation can be classified as a ferroelectric phase transition according to the Aizu notation $2/mF2$ (Figure S3).[39] The symmetry-breaking transformation from phase α to β was further confirmed by second harmonic

https://doi.org/10.1021/acs.chemmater.5c00335
Chem. Mater. 2025, 37, 2953−2963

generation (SHG) measurements. As shown in Figure 3, the SHG signal was detected from the ambient pressure phase α in the range of 400−1100 nm. However, when the pressure was increased to 0.12 GPa, the signal disappeared. Upon releasing the pressure to 0.1 MPa, the SHG signal became observable again, thereby verifying the acentric-to-centric phase transformation of compound **1** under compression. In contrast to other reported crystals,[40,41] compound **1** exhibits rather rare SHG "on−off" switching at the megapascal pressure range, suggesting its potential for application in pressure-controlled SHG switches in deep-sea environments.

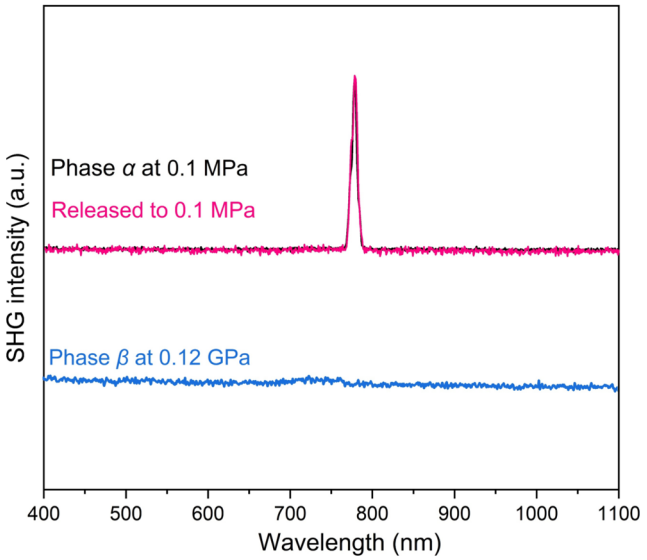

Figure 3. Second harmonic generation (SHG) signal of compound **1**. The phase α at 0.1 MPa prior to the compression and the released data at 0.1 MPa are plotted in black and pink, respectively. The signal corresponding to phase β at 0.12 GPa is shown in blue.

As shown in Figure 2b, a distinct volume collapse of ∼ 2.4% appears during the phase α-β transformation, indicative of the first-order phase transition (Figure 2b). In the high-pressure SXRD measurements, two different single crystals of compound **1** were loaded in the diamond anvil cell chambers, with the initial organic cations adopting M- or P-helicity and were compressed to 10.83 GPa (crystal A) and 8.83 GPa (crystal B), respectively. The obtained SXRD results indicate that no discernible differences in the lattice parameters at comparable pressures are observed (Tables S2 and S3). Subsequent to the gradual release of these maximum pressures to ambient conditions, it was observed that the phase transformation is reversible (Table S1). Phase β remains stable over a wide pressure range, at least to the experimental limit of 10.83 GPa. In phase β, the lattice parameters exhibit anisotropic compressibility (Figures 2a and S4). The magnitude of the strain tensor β_3 is 14.7(21) TPa^{-1}, which is inclined by ∼18.0° to the a axis, and it is ∼1.8 times of that approximately along the c axis (where β_1 equals 8.2(9) TPa^{-1}, inclined by 30.2°). The weakest compressibility is observed along the b axis, with compressibility coefficient β_2 of 4.6(6) TPa^{-1}, which is about three times smaller than β_3 (see Table S3). The formula-unit volume data (V/Z) of phase β were well fitted to the third-order Birch−Murnaghan equation of state, yielding a zero-pressure bulk modulus B_0 of 11.4(8) GPa and pressure derivative B' of 5.9(5). This magnitude is comparable to those reported for 1D hybrid halides.[42,43]

To understand the exceptional transformation to the racemate, along with the associated conformational changes in the organic cations $(NH_3(CH_2)_2S{-}S(CH_2)_2NH_3)^{2+}$ under compression, we have determined the crystal structures of compound **1** at various pressures. In phase α, the torsion angle C−S−S−C within the organic cation at ambient pressure is approximately −85° for M- or P-helicity crystals (Figure 1a), which is larger than that observed for the 2D hybrid lead halide $[(NH_3(CH_2)_2S{-}S(CH_2)_2NH_3)]PbI_4$ (−75°).[44] The torsion angle increases to −90.1(16)° in phase β at 0.43 GPa and gradually increases to − 96.7(25)° as the pressure reaches 10.83 GPa (Figures 1d and S6b). Furthermore, we have refined the decompression SCXRD data at 0.1 MPa and found that the values of the Hooft parameter close to 0 (e.g., −0.015(5) for M-helicity, crystal A).[45] These findings reveal the reversibility of the conformational changes of the organic cations. Moreover, the transition also induces pronounced changes in the $-C(4)H_2-N(2)H_3$ fragments, which exhibit a disordered state in the high-temperature phase. However, under external pressure, half of the organic molecules with left-handed helical form (M-helicity) in crystal A undergo conformational changes to right-handed form with the $-C(4)H_2-N(2)H_3$ groups ordered (here C(4) atom resembles a chiral carbon, Figure 1a). The torsion angle N(2)−C(4)−C(3)−S(1) equals 59.9(7)° (P-helicity) at ambient pressure, it abruptly increases to 161.3(14)° at 0.43 GPa following the phase transformation. It remains roughly unchanged as the pressure increases to ∼6.0 GPa and starts to reduce considerably and finally reaching 9.5(31)° at 10.83 GPa. Such significant directional alterations of $-C(4)H_2-N(2)H_3$ fragments are primarily due to changes in the packing arrangements of the organic cations, which must adjust their positions to accommodate the available space within the constrained lattice (Figures 2d and S5). Through theoretical calculations, it was determined that the energy difference between phases α and β is 4.74 eV/cell. This energy difference can be overcome by external work ($P\Delta V$), resulting in the formation of the β phase. Under compression, the screw-like organic cations act as molecular springs and thus undergo significant conformational alterations in the β phase, which ultimately influence the geometry of 1D zigzag chain by tilting the PbI_6 octahedra out of the ab plane. The extent of the PbI_6 octahedral distortion can be qualified by the quadratic elongation ($\langle\lambda\rangle$) and bond angle variance (σ_θ^2), which are defined as follows[46]

$$\langle\lambda\rangle = \sum_{i=1}^{6} (l_i/l_0)^2/6 \quad (1)$$

$$\sigma_\theta^2 = \sum_{i=1}^{12} (\theta_i - 90^\circ)^2/11 \quad (2)$$

where l_i is the Pb−I bond length, l_0 is the average Pb−I bond length, and θ_i is the I−Pb−I bond angle of neighboring iodides. In phase α, the Pb1−I4 and Pb1−I4′ bond distances are 3.2419(15) and 3.2271(16) Å and they increase slightly to 3.262(2) and 3.279(2) Å at 0.43 GPa after phase transformation (Figure 2c,d). Meanwhile, the octahedral distortion parameters <λ> and σ_θ^2 for the PbI_6 octahedra in phase α are (0.9969, 12.08) and subsequently increase to (1.0003, 13.44) during the phase transition. Upon compression, the Pb1−I4

https://doi.org/10.1021/acs.chemmater.5c00335
Chem. Mater. 2025, 37, 2953−2963

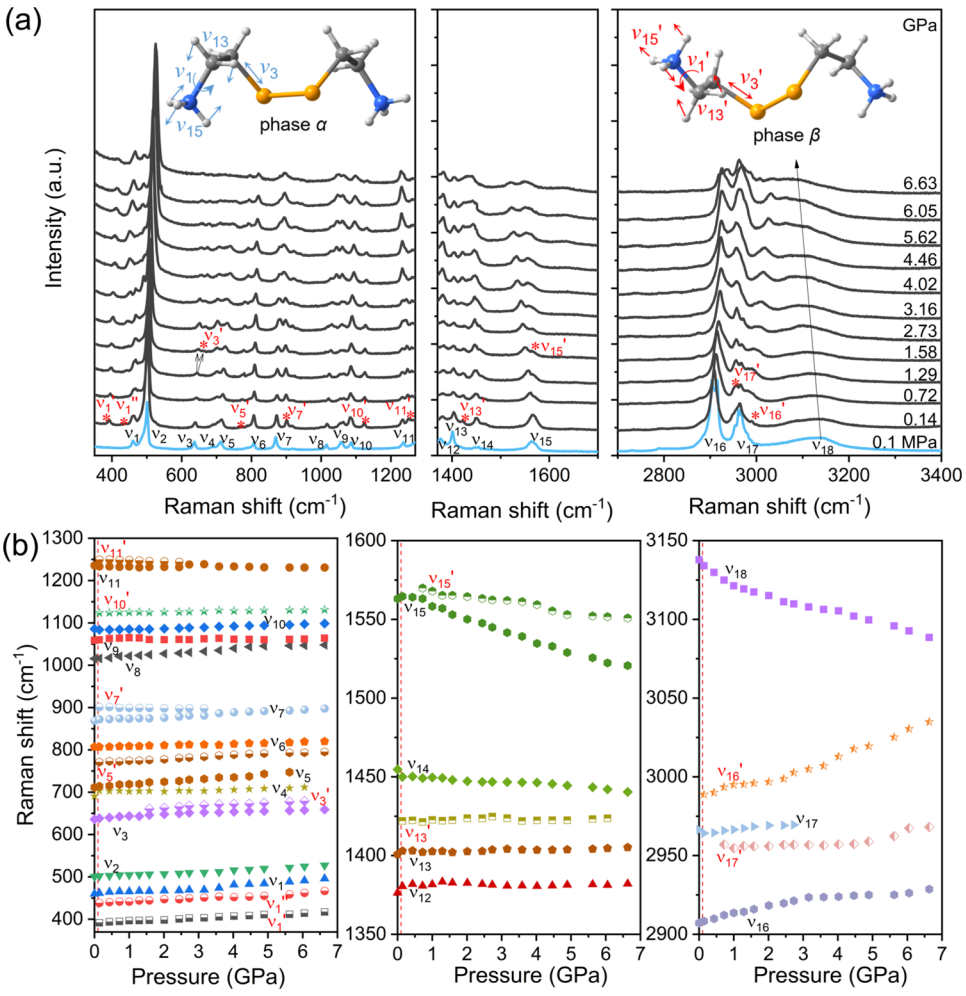

Figure 4. Raman spectra of compound **1** at different pressures. (a) Selected Raman spectra upon compression to 6.63 GPa. (b) Evolution of the Raman modes under pressure. The inset highlights the newly emerged selective vibration modes during the phase transition.

bond length gradually decreases from 3.262(2) Å (at 0.43 GPa) to 2.982(5) Å (at 10.83 GPa), whereas the apical Pb1−I3 bond length slightly changes by ∼3.0%. Furthermore, the <λ> parameter slightly decreases to 1.0000 at 10.83 GPa due to the decrease in the Pb−I bond distances under pressure. The Pb1−I4′−Pb1′ angle between the neighboring PbI_6 octahedron along the *b* axis does not undergo abrupt changes during the phase transformation, indicating that the inorganic framework is maintained. For example, the Pb−I−Pb angle is 169.95(5)° at 0.1 MPa and it decreases slightly to 168.4(1)° at 0.43 GPa after the phase α-β transition. Subsequently, it continues to decrease slightly until ∼6.0 GPa and then ultimately increases to 176.2(1)° at 10.83 GPa (Figure 2d). For the bond angle variance σ_θ^2, it increases monotonically until ∼6.0 GPa and then undergoes an abrupt increase due to conformational changes in the organic cations. These changes lead to substantial distortions in the PbI_6 octahedra through strong H···I interactions as described above. Therefore, it is emphasized that the organic−inorganic interactions play a significant role in inducing distortions in the 1D PbI_5 chains under pressure.

The uncommon transformation of a conglomerate into a racemate results in new hydrogen bonding patterns due to the directional changes of $-C(4)H_2-N(2)H_3$ ethylammonium groups within the flexible organic cations in phase β (see Figures 2 and S1). At ambient pressure, the ammonium $-NH_3$ head and tail groups separately interact with two PbI_6 octahedra (2.775−2.982 Å for N(1), 2.686−2.868 Å for N(2)) and they elongate at 0.43 GPa (2.992−3.063 Å for N(1), 2.745−3.021 Å for N(2)), indicative of the NH···I interactions became weaker in phase β (Figure S6a). As pressure increases, the crystal structure becomes more compacted in phase β, with more NH···I contacts forming and new CH···I interactions from the $-C(4)H_2$ groups emerging due to the directional alterations of $-C(4)H_2-N(2)H_3$ groups (Figure S7b,c). For example, the $-N(2)H_3$ group interacts with three PbI_6 octahedra, with distances ranging from 2.551 to 2.888 Å, whereas the CH···I interactions are significantly stronger (2.311−2.786 Å). These enhanced NH···I and CH···I interactions are likely responsible for the large distortions of the PbI_6 octahedra, as displayed in Figure 2f. The evolution of organic−inorganic interactions in both phases α and β is further illustrated by the differences in Hirshfeld surfaces and two-dimensional (2D) fingerprint plots (Figure S7). In phase α, large red spots appear around the $-NH_3$ groups, indicating the presence of strong H···I interactions (Figure S7a). In phase β, large conformational changes of the organic cations give rise to distinct Hirshfeld surfaces (Figure S7b). As pressure increases, the distances of H···I interactions are gradually shortened, characterized by large red spots on the Hirshfeld surface at 10.83 GPa (even around the $-CH_2$ groups). The H···I interactions correspond

https://doi.org/10.1021/acs.chemmater.5c00335
Chem. Mater. 2025, 37, 2953−2963

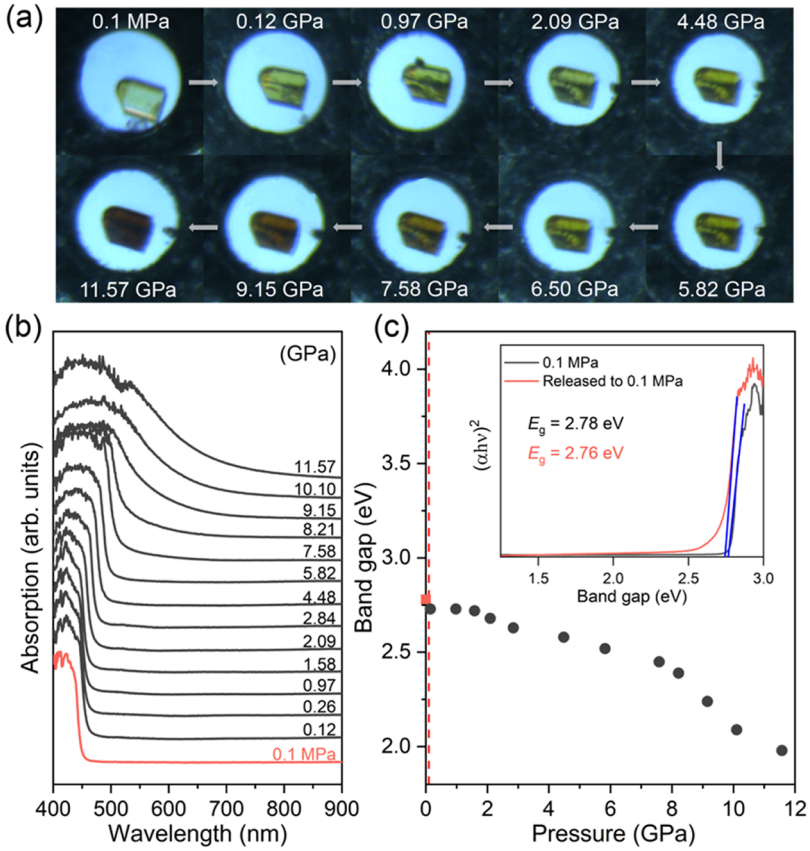

Figure 5. Optical properties of compound **1** under pressure. (a) Optical images of a single crystal under compression. Note that the alterations of the single crystal surface are likely caused by the ferroelectric phase transition. (b) Evolution of the absorption spectra under pressure. (c) Variations in the bandgap of the sample under compression. The inset shows the bandgap of the sample at 0.1 MPa (phase α) and data released to ambient pressure.

to a sharp spike in the 2D fingerprint plots, with a relative contribution of 59.7% at 0.43 GPa, which then gradually decreases to 54.2% as the pressure increases to 10.83 GPa (Figure S7).

The occurrence of the $\alpha \rightarrow \beta$ phase transformation is also clearly evident in the Raman spectra under high pressure, as indicated by significant changes in the Raman modes of the organic cations (see Figure 4). The Raman modes of sample **1** at ambient pressure are assigned according to previous studies (Table S4).[12,44,47,48] For phase α at 0.1 MPa, the Raman mode designated as ν_1, locates at 460.1 cm^{-1} and corresponds to the torsional vibrations of NH_3^+. The Raman mode ν_2, exhibiting the strongest intensity in the low frequency region, is associated with S−S stretching vibrations. Another mode ν_3 at 636.1 cm^{-1} is associated with C−S stretching vibrations. The Raman peaks within the 700 to 1270 cm^{-1} range can be categorized as follows: CH_2 rocking vibrations (modes ν_4 and ν_5), C−N stretching vibrations (ν_6 and ν_7 modes), CH_2 twisting vibrations (modes ν_8 and ν_9), and CH_2−NH_3 rocking vibrations (modes ν_{10} and ν_{11}). Meanwhile, the Raman peaks in the 1370−1700 cm^{-1} region are primarily composed of bending vibrations of $-CH_2$ and $-NH_3$, while those in the 2700−3400 cm^{-1} region are assigned to N−H stretching, C−H stretching, and O−H stretching modes (see Table S4 for details). As the pressure was gradually increased to 0.14 GPa, a number of new Raman peaks emerged in the spectra, indicative of the occurrence of the phase transition (Figure 4a). For example, the new modes ν_1', ν_7' and ν_{11}' are associated with the NH_3^+ torsional vibration, C−N stretching and the CH_2−NH_3 rocking vibrations, respectively, revealing significant conformational changes in the cystamine cations at 0.14 GPa. Upon compression, the majority of Raman modes shift to higher wavenumbers (blue shift) due to the compressed lattice. However, some Raman peaks were observed to demonstrate the opposite trend. For example, the Raman modes ν_{14}, ν_{15} and ν_{18} at 1450.0, 1564.6, and 3134.0 cm^{-1} at 0.14 GPa correspond to symmetric $-NH_3$ bending, asymmetric $-NH_3$ bending and O−H stretching vibrations, respectively. These unusual redshifts reveal enhanced NH···I and OH···I hydrogen bonding between the cystamine (hydronium) cations and the inorganic framework. Previous studies have demonstrated that the Raman spectra of the C−S−S−C moiety in different conformations exhibit significant distinctions. The *ggg*-type conformer manifests a single marker at ∼630 cm^{-1}, whereas the *ggt*-type conformer exhibits a double marker at ∼630 and ∼660 cm^{-1}.[49] Therefore, it can be argued that the appearance of the new Raman peak at 661.1 cm^{-1} (mode ν_3') at 1.58 GPa can be assigned to C−S stretching vibrations, revealing the torsion angle changes of the C−S−S−C moiety under pressure. These observations demonstrate that compound **1** undergoes significant conformational changes in the organic cations during the conglomerate to racemate transformation, which is well consistent with the aforementioned SXRD data.

To investigate the variation in the bandgap of **1** under pressure, *in situ* UV−vis absorption spectra were collected up to 11.57 GPa at room temperature (Figure 5). The Tauc plots

https://doi.org/10.1021/acs.chemmater.5c00335
Chem. Mater. 2025, 37, 2953−2963

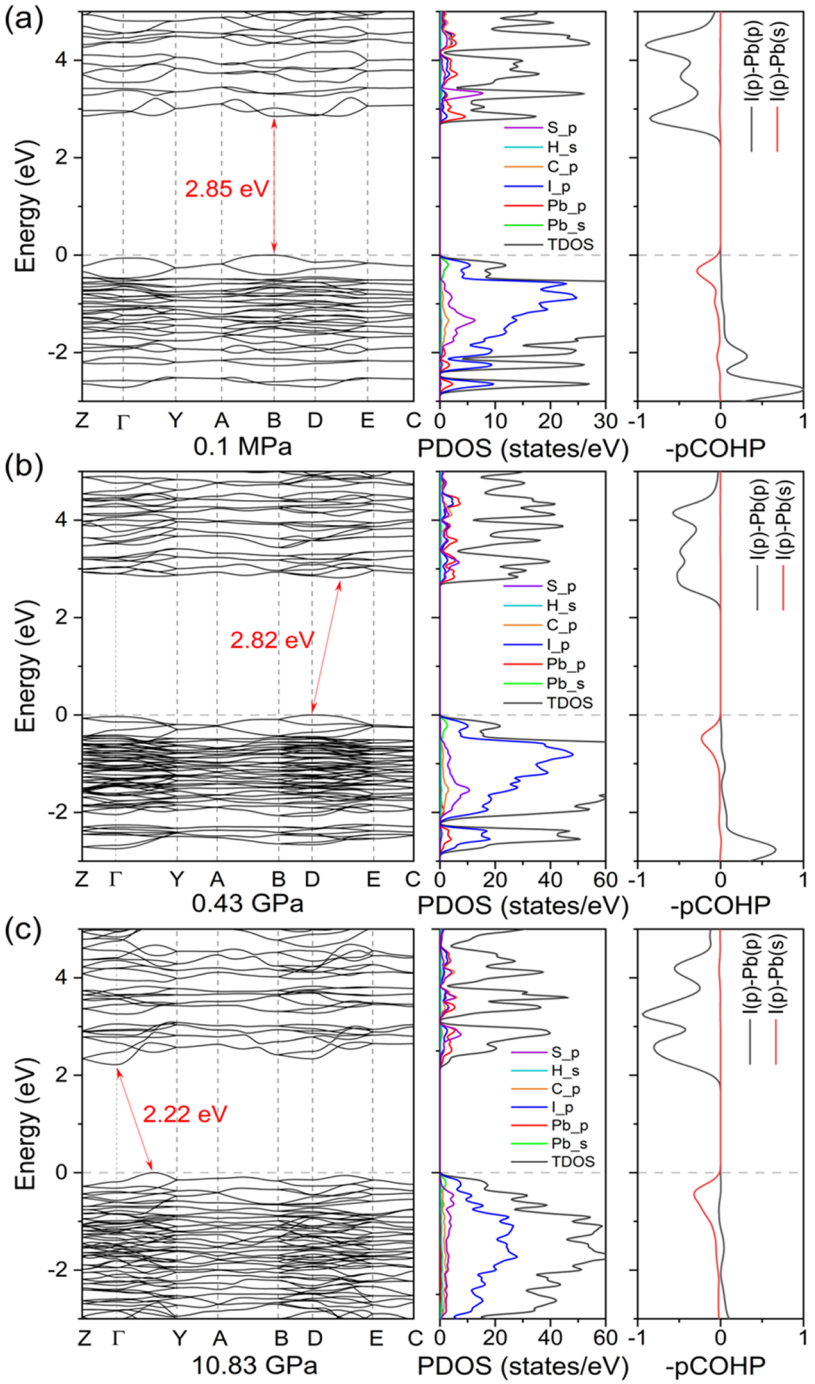

Figure 6. Electronic structures of **1** at selective pressures. (a) phase α at 0.1 MPa; (b) phase β at 0.43 GPa and (c) 10.83 GPa. Positive and negative -pCOHP indicates bonding and antibonding interactions, respectively. The Fermi level is set to 0 eV.

for the bandgap calculations under different pressures are shown in Figure S8. At ambient pressure, the sample appears light-yellow with a bandgap of 2.78 eV (phase α). The absorption edge exhibits a slight redshift during the phase α-β transition, with the bandgap decreasing to 2.73 eV at 0.12 GPa (phase β). As the pressure increases to 11.57 GPa, the color of the single crystal gradually darkens and changes to dark brown. Consequently, the bandgap decreases monotonically to 1.98 eV. The reduction in bandgap arises from the decrease in the Pb−I bond distances under compression, as observed in other reported low-dimensional halides.[50−52] As shown in Figure 5c, the rate of bandgap reduction increases significantly when the pressure exceeds 6.0 GPa. This feature is most likely attributed to the shortened Pb−I bond lengths under compression (as shown in Figure 2c−f). Upon releasing the pressure to 0.1 MPa, the measured bandgap equals 2.76 eV, slightly smaller than the initial value, indicative of the reversibility of the phase transformation and consistent with the results observed in the SXRD measurements (Table S1).

To elucidate the changes of optical behavior of compound **1**, the electronic structures of phases α and β at selected pressures were calculated using the PBE functional. As shown in Figure 6a, phase α at 0.1 MPa is a direct semiconductor with the conduction band minimum (CBM) and valence band

https://doi.org/10.1021/acs.chemmater.5c00335
Chem. Mater. 2025, 37, 2953−2963

maximum (VBM) at the B point of the first Brillouin zone. The calculated bandgap of 2.85 eV is in good agreement with the experimental value. As observed in the reported hybrid halides,[53,54] the VBM of the α phase is predominantly composed of I-5p and Pb-6s orbitals, while the states near the CBM are primarily derived from Pb-6p and I-5p orbitals, indicating a Pb^{2+} ($6s^2$) configuration. The projected crystal orbital Hamilton population (pCOHP) analysis shows a strong antibonding interaction between Pb-6s and I-5p at the top of the valence band, which is commonly observed in the systems containing lone-pair electrons.[55] After the phase transformation, an indirect electronic bandgap is observed. The band dispersion and main constituents of VBM in phase β at 0.43 GPa remain largely unchanged from phase α; however, the S-p orbital begins to shift downward, contributing more to CBM, likely as a result of the conformational changes of the organic cations. As the pressure increases, the Pb−I bond lengths are gradually shortened, thereby increasing the orbital overlap between Pb-6s and I-5p as well as that between Pb-6p and I-5p, which leads to broadening of the valence and conduction bands and consequently, a smaller electronic bandgap (from 2.82 eV at 0.43 GPa to 2.22 eV at 10.83 GPa).[56] Interestingly, the locations of the CBM and VBM shift to the Γ point (0, 0, 0) and the midpoint of the line (0, 0.32, 0) between the Γ and Y points at 10.83 GPa, respectively. All calculated bandgaps are consistent with the trend observed in experimental results. Meanwhile, the primary contributions of the CBM are changed to Pb-6p orbital and VBM remains the same as that of 0.43 GPa. The analysis of the projected density of states under variable pressures indicates that the energy bands near the Fermi level of compound **1** are predominantly influenced by the Pb and I atoms. In contrast, alterations in the organic components appear to exert minimal impact on the overall energy band structures.

The electron localization function (ELF) was computed for phases α and β to analyze Pb−I bond variations within PbI_6 octahedra. Figure S9 presents spherical ELFs around Pb atoms in both phases, lacking a fixed orientation, indicating a nonstatic spherical distribution of lone pair electrons.[57,58] The ELF value for Pb−I approaches zero, with electrons predominantly localized on I atoms, fully occupying the 5p orbital. This indicates significant electron delocalization and predominantly ionic interactions between Pb and I within the inorganic framework. Under compression, the electrostatic potential overlap between Pb and I atoms intensifies, strengthening their interactions and shortening the Pb−I bond lengths.

CONCLUSIONS

In summary, we report the conglomerate-to-racemate transition in the 1D chiral hybrid halide **1**, facilitated by the incorporation of flexible cystamine cations under a low hydrostatic pressure of ∼0.1 GPa. The reversible acentric-to-centric phase transition is accompanied by significant conformational changes in the cystamine cations and the disappearance of SHG behavior. In the high-pressure racemic phase β, the cystamine cations deform considerably under compression, resembling a compressed mechanical spring. The deformation leads to large distortions in the 1D zigzag PbI_5 chains through strong H···I organic−inorganic interactions. Intriguingly, the transformation induces a slight reduction in the bandgap, indicating that the electronic structures near the Fermi level are primarily derived from the corner-sharing PbI_6 octahedra inorganic framework, with minor contributions from the organic moieties. The reversible acentric-to-centric phase transition of compound 1 at ∼100 MPa makes the material an excellent candidate for a variety of deep-sea applications, including use in optical switches for underwater communication networks and pressure-sensitive sensors for submersible instruments. With potential advantages including high on/off contrast in SHG output and fast reversible switching, these devices promise energy-efficient and robust performance. However, the practical deployment of these devices will require careful attention to packaging, long-term cycling stability, precise integration with optical systems, and control of hysteresis effects. Addressing these challenges will be significant to making the application prospects both practical and attractive for deep-sea environments. This study offers novel insights into the pressure-induced conglomerate to racemate transformation in solid crystalline halides, thereby providing an approach to manipulating molecular chirality structures in hybrid halides through the incorporation of flexible disulfide-based molecules with a low energy barrier of C−S−S−C conformations.

EXPERIMENTAL SECTION

Synthesis of Single Crystals of 1. The $[NH_3(CH_2)_2S-S(CH_2)_2NH_3]PbI_5{\cdot}H_3O$ (**1**) single crystals were synthesized via a solvothermal method in a 25 mL hydrothermal reaction autoclave, as previously reported.[30] 0.4 mmol cystamine dihydrochloride $H_2N(CH_2)_2SS(CH_2)_2NH_2{\cdot}2HCl$ (98%, Macklin) was dissolved in the 4 mL acetonitrile with stirring, followed by the addition of 0.4 mmol PbI_2 (99.9%, Aladdin), and the mixture was stirred until all components were dissolved. Subsequently, 1 mL of concentrated HI was added dropwise and stirred for 10 min. Finally, the autoclave was sealed, heated to 353 K for 30 min, maintained at this temperature for 2 h, and then cooled to room temperature at a rate of 1 K/h. The yellow, needle-shaped single crystals were finally obtained by rapidly washing with cold ethyl acetate.

Single-Crystal X-ray Diffraction Measurements. Single-crystal X-ray data for compound 1 were collected using a Bruker D8 Quest diffractometer with a Phonon III detector and four-cycle kappa geometry, and Incoatec IμS 3.0 Mo Kα microfocus (λ = 0.71073 Å). High-pressure data were collected by using eight different phi scans, with the exposure time of 10−15 s for each frame. Two different single crystals, A (dimensions: 0.096 × 0.060 × 0.030 mm^3 for M helicity) and B (dimensions: 0.095 × 0.092 × 0.053 mm^3 for P helicity), were employed for the high-pressure single-crystal X-ray diffraction measurements. A symmetric diamond anvil cell (DAC) with an aperture angle of 85° and a culet diameter of 400−500 μm, was mounted on the goniometer head. Tungsten foils were initially preintended to a thickness of ∼80 μm and the holes were subsequently drilled to diameter of ∼220 μm by a UV laser. The ruby fluorescence method was employed to calibrate the pressure with an accuracy of 0.03−0.05 GPa before and after each X-ray data collection.[59] To ensure good hydrostaticity, daphne oil 7575 was used as pressure-transmitting medium (PTM).[60] Single crystal diffraction data were measured from 0.1 MPa to 10.83 GPa at 15 pressure points, with seven points for crystal A and eight points for crystal B. To confirm the structural stability of crystal A at low temperatures, single-crystal X-ray data were also collected at 100 K. Data collection, indexing, and reduction were performed using the APEX5. The structure was solved with the SHELXS-1997 using direct methods and refined with the XL refinement package using least-squares minimization.[61] Selected crystallographic details at variable pressures are presented in Tables S1 and S2. Furthermore, the EoSFit7c software was used to perform least-squares fitting of $P-V$ data from the third-order Birch−Murnaghan equation of states (EoS) for phase β of compound 1.[62]

https://doi.org/10.1021/acs.chemmater.5c00335
Chem. Mater. 2025, 37, 2953−2963

High-Pressure Second Harmonic Generation Measurements. Second harmonic generation (SHG) measurements were conducted to confirm the acentric-to-centric transformation of compound 1 under compression. The measurements were carried out using a home-designed goLite Solution-NLO optical system. A pulsed 1550 nm fiber laser was used as the excitation light source. A 50× objective was used to focus the laser, producing a laser spot with a diameter of 10 μm. A spectrometer (NVOA2S-EX) was used to collect the SHG signal. Due to the moderate transition pressure, silicone oil was used as the PTM to provide good hydrostatic environment (hydrostatic limit: ∼1.0 GPa). The system was validated with a small KH_2PO_4 (KDP) single crystal prior to starting the measurements.

High-Pressure Raman Spectroscopy Measurements. High-pressure *in situ* Raman spectroscopy experiments were conducted in a symmetric DAC using ultralow fluorescence type IIa diamonds with a culet diameter of 350 μm. Daphne oil 7575 was employed as the PTM. High-pressure Raman spectra were recorded using a 532 nm green laser. Before the Raman measurements, the system was calibrated using a silicon wafer. The Raman spectra were collected in the range of 300−4000 cm^{-1} with the resolution of approximately 1 cm^{-1}.

High-Pressure UV−vis Absorption Measurements. High-pressure *in situ* UV−vis absorption measurements of compound 1 were performed in a home-built spectroscopy system using a deuterium-halogen lamp 2-in-1 light source, ranging from 300 and 900 nm. Daphne oil 7575 was used as the PTM. The direct and indirect band gaps were determined by extrapolating the linear regions of the $(\alpha h\nu)^2$ and $(\alpha h\nu)^{1/2}$ versus $h\nu$ curves, where α is the absorption coefficient, h is Planck's constant, and ν is the photon frequency.

Theoretical Calculations. First-principles calculations of the pressure-dependent density of states, band structure, electron localization function (ELF) and crystal orbital Hamilton population (COHP) were carried out using Vienna Ab initio Simulation Package (VASP) based on plane wave pseudo potential methods.[63−69] All theoretical calculations were performed using projected augmented wave (PAW) formalism of the Kohn−Sham density functional theory with generalized gradient approximation (GGA) for exchange correlation, as described by Perdew, Burke, and Ernzerhof (PBE).[70] A plane-wave basis set with an energy cutoff of 500 eV was used in all calculations. For structural self-consistency, the 5 × 6 × 4 and 4 × 6 × 3 k-points were utilized for phases α and β, respectively, with the Hellmann−Feynman force acting on each atom being less than 0.001 eV/Å. Based on the self-consistent results, the "LELF" command is invoked to obtain the ELF information through a static calculation, and then the visualization of the ELF is realized using the VESTA software. For electronic structures and energy calculations, a denser Monkhorst−Pack grid of 8 × 9 × 6 and 5 × 8 × 4 in the Brillouin zone was adopted for phases α and β, respectively. High-symmetry points of Z, Γ, Y, A, B, D, E and C in the Brillouin zone correspond to (0, 0, 0.5), (0, 0, 0), (0, 0.5, 0), (−0.5, 0.5, 0), (−0.5, 0, 0), (−0.5, 0, 0.5), (−0.5, 0.5, 0.5), and (0, 0.5, 0.5) points for phases α and β for band structure calculations, respectively. The following orbitals were explicitly treated as valence electrons: Pb $5d^{10}6s^26p^2$, I $5s^25p^5$, S $3s^23p^4$, O $2s^22p^4$, C $2s^22p^2$, N $2s^22p^3$, and H $1s^1$. The COHP analysis were computed with the Lobster code via transformation of the plane wave functions obtained by VASP into a localized basis set Slater-Type orbitals (STO).[71] All calculations were performed using the experimental unit-cell lattice parameters obtained from the high-pressure SXRD measurements.

■ ASSOCIATED CONTENT

Supporting Information

The Supporting Information is available free of charge at https://pubs.acs.org/doi/10.1021/acs.chemmater.5c00335.

Crystal structures analysis at various pressures; variations in the conformational changes of the cystamine cations under pressure; details of the crystallographic data; and assignments of the Raman spectra (PDF)

Accession Codes

CCDC 2418052−2418064 contain the supplementary crystallographic data for this paper. These data can be obtained free of charge via www.ccdc.cam.ac.uk/data_request/cif, by emailing data_request@ccdc.cam.ac.uk, or by contacting The Cambridge Crystallographic Data Centre, 12 Union Road, Cambridge CB2 1EZ, UK; fax: + 44 1223 336033.

■ AUTHOR INFORMATION

Corresponding Author

Weizhao Cai − *School of Materials and Energy, University of Electronic Science and Technology of China, Chengdu 611731, China;* orcid.org/0000-0001-7805-2108; Email: wzhcai@uestc.edu.cn

Authors

Wenbo Qiu − *School of Materials and Energy, University of Electronic Science and Technology of China, Chengdu 611731, China*

Weilong He − *School of Materials and Energy, University of Electronic Science and Technology of China, Chengdu 611731, China*

Yu Liu − *School of Materials and Energy, University of Electronic Science and Technology of China, Chengdu 611731, China*

Boyang Fu − *School of Materials and Energy, University of Electronic Science and Technology of China, Chengdu 611731, China*

Weiyi Wang − *School of Materials and Energy, University of Electronic Science and Technology of China, Chengdu 611731, China*

Jiangang He − *Key Laboratory of Advanced Materials and Devices for Post-Moore Chips, Ministry of Education and School of Mathematics and Physics, University of Science and Technology Beijing, Beijing 100083, China*

Luhong Wang − *Shanghai Advanced Research in Physical Sciences, Shanghai 201203, China;* orcid.org/0000-0001-8851-4935

Haozhe Liu − *Center for High Pressure Science and Technology Advanced Research, Beijing 100094, China;* orcid.org/0000-0001-5720-2031

Complete contact information is available at: https://pubs.acs.org/10.1021/acs.chemmater.5c00335

Notes

The authors declare no competing financial interest.

■ ACKNOWLEDGMENTS

We acknowledge the financial support from the National Natural Science Foundation of China (No. 12274062). This work was partially carried out at the Synergetic Extreme Condition User Facility (SECUF).

■ REFERENCES

(1) Sui, J.; Wang, N.; Wang, J.; Huang, X.; Wang, T.; Zhou, L.; Hao, H. Strategies for Chiral Separation: from Racemate to Enantiomer. *Chem. Sci.* **2023**, *14*, 11955−12003.

(2) Jacques, J.; Collet, A.; Wilen, S. H. *Enantiomers, Racemates and Resolutions*; Krieger Publishing Company: Malabar, FL, 1994.

(3) Xue, W.; Ronson, T. K.; Lu, Z.; Nitschke, J. R. Solvent Drives Switching between Λ and Δ Metal Center Stereochemistry of M_8L_6 Cubic Cages. *J. Am. Chem. Soc.* **2022**, *144*, 6136−6142.
(4) Sakata, Y.; Chiba, S.; Akine, S. Transient Chirality Inversion During Racemization of A Helical Cobalt(III) Complex. *Proc. Natl. Acad. Sci. U.S.A.* **2022**, *119*, No. e2113237119.
(5) Matsumura, K.; Kinjo, K.; Tateno, K.; Ono, K.; Tsuchido, Y.; Kawai, H. *M/P* Helicity Switching and Chiral Amplification in Double-Helical Monometallofoldamers. *J. Am. Chem. Soc.* **2024**, *146*, 21078−21088.
(6) Huck, N. P. M.; Jager, W. F.; de Lange, B.; Feringa, B. L. Dynamic Control and Amplification of Molecular Chirality by Circular Polarized Light. *Science* **1996**, *273*, 1686−1688.
(7) Ikeda, K.; Liu, W.; Shen, Y. R.; Uekusa, H.; Ohashi, Y.; Koshihara, S.-y. Photo-Induced Chirality Switching in a Cobaloxime Complex Crystal. *J. Chem. Phys.* **2005**, *122*, No. 141103.
(8) Rickhaus, M.; Mayor, M.; Juríček, M. Strain-induced Helical Chirality in Polyaromatic Systems. *Chem. Soc. Rev.* **2016**, *45*, 1542−1556.
(9) Cai, W.; Marciniak, J.; Andrzejewski, M.; Katrusiak, A. Pressure Effect on D,L-Mandelic Acid Racemate Crystallization. *J. Phys. Chem. C* **2013**, *117*, 7279−7285.
(10) Marciniak, J.; Andrzejewski, M.; Cai, W.; Katrusiak, A. Wallach's Rule Enforced by Pressure in Mandelic Acid. *J. Phys. Chem. C* **2014**, *118*, 4309−4313.
(11) Moggach, S. A.; Allan, D. R.; Parsons, S.; Sawyer, L.; Warren, J. E. The Effect of Pressure on the Crystal Structure of Hexagonal L-Cystine. *J. Synchrotron Radiat.* **2005**, *12*, 598−607.
(12) Song, M.; Li, W.; Zhang, X.; Liu, J.; Li, K.; Zhang, H. Structural Stability of L-Cystine under Extreme Conditions. *ACS Earth Space Chem.* **2021**, *5*, 1525−1534.
(13) Roszak, K.; Katrusiak, A. High-Pressure Crystallization and Thermodynamic Stability Study on the Resolution of High-Density Enantiomers from Low-Density Racemates. *Org. Lett.* **2023**, *25*, 37−41.
(14) Ostrowska, K.; Kropidłowska, M.; Katrusiak, A. High-Pressure Crystallization and Structural Transformations in Compressed *R,S*-Ibuprofen. *Cryst. Growth Des.* **2015**, *15*, 1512−1517.
(15) Roszak, K.; Katrusiak, A. High-Pressure and Temperature Dependence of the Spontaneous Resolution of 1,1′-Binaphthyl Enantiomers. *Phys. Chem. Chem. Phys.* **2018**, *20*, 5305−5311.
(16) Yang, C.-K.; Chen, W.-N.; Ding, Y.-T.; Wang, J.; Rao, Y.; Liao, W.-Q.; Tang, Y.-Y.; Li, P.-F.; Wang, Z.-X.; Xiong, R.-G. The First 2D Homochiral Lead Iodide Perovskite Ferroelectrics: [*R*- and *S*-1-(4-Chlorophenyl)ethylammonium]$_2$PbI$_4$. *Adv. Mater.* **2019**, *31*, No. 1808088.
(17) Liao, W.-Q.; Zhang, Y.; Hu, C.-L.; Mao, J.-G.; Ye, H.-Y.; Li, P.-F.; Huang, S. D.; Xiong, R.-G. A Lead-Halide Perovskite Molecular Ferroelectric Semiconductor. *Nat. Commun.* **2015**, *6*, No. 7338.
(18) Ge, F.; Cheng, P.; Li, Q.; Xu, J.; Bu, X.-H. Achiral Fluorinated Aromatic Ligands Based Chiral Hybrid Antimony Halides with High-Efficiency Second-Harmonic Generation. *Adv. Opt. Mater.* **2023**, *11*, No. 2301040.
(19) Long, G.; Sabatini, R.; Saidaminov, M. I.; Lakhwani, G.; Rasmita, A.; Liu, X.; Sargent, E. H.; Gao, W. Chiral-Perovskite Optoelectronics. *Nat. Rev. Mater.* **2020**, *5*, 423−439.
(20) Ji, X.; Geng, S.; Zhang, S.; Gong, Y.; Zhang, X.; Li, R.; Liu, Y.; Chen, J.; Chen, R.; Xiao, Z.; Mao, L. Chiral 2D Cu(I) Halide Frameworks. *Chem. Mater.* **2022**, *34*, 8262−8270.
(21) Pan, R.; Tao, S.; Wang, K.; Yu, Z.-G. Experimental and Theoretical Studies of Magnetic Circular Dichroism for Chiral Lead Halide Perovskites. *Chem. Mater.* **2023**, *35*, 1667−1673.
(22) Li, Z.-G.; Dong, X.-H.; Song, H.-P.; Huang, S.-S.; Hu, H.; Zhang, Y.; Wu, X.; Li, W.; Bu, X.-H. Chirality-Mediated 1D-to-2D Phase Transition in Hybrid Lead Halide Perovskites. *J. Am. Chem. Soc.* **2024**, *146*, 27946−27955.
(23) Sun, M.-E.; Wang, Y.; Wang, F.; Feng, J.; Wang, L.; Gao, H.; Chen, G.; Gu, J.; Fu, Y.; Bu, K.; et al. Chirality-Dependent Structural Transformation in Chiral 2D Perovskites under High Pressure. *J. Am. Chem. Soc.* **2023**, *145*, 8908−8916.
(24) Gao, F.-F.; Song, H.; Li, Z.-G.; Qin, Y.; Li, X.; Yao, Z.-Q.; Fan, J.-H.; Wu, X.; Li, W.; Bu, X.-H. Pressure-Tuned Multicolor Emission of 2D Lead Halide Perovskites with Ultrahigh Color Purity. *Angew. Chem., Int. Ed.* **2023**, *62*, No. e202218675.
(25) Zheng, H.; Zhang, R.; Wu, X.; Zhang, Q.; Wu, Z.; Wong, W. P. D.; Chen, J.; Xu, Q.-H.; Loh, K. P. Strain-Driven Solid−Solid Crystal Conversion in Chiral Hybrid Pseudo-Perovskites with Paramagnetic-to-Ferromagnetic Transition. *J. Am. Chem. Soc.* **2023**, *145*, 3569−3576.
(26) Steudel, R. Properties of Sulfur-Sulfur Bonds. *Angew. Chem., Int. Ed. Engl.* **1975**, *14*, 655−664.
(27) Rimer, J. D.; An, Z.; Zhu, Z.; Lee, M. H.; Goldfarb, D. S.; Wesson, J. A.; Ward, M. D. Crystal Growth Inhibitors for the Prevention of L-Cystine Kidney Stones Through Molecular Design. *Science* **2010**, *330*, 337−341.
(28) Bi, W.; Louvain, N.; Mercier, N.; Luc, J.; Rau, I.; Kajzar, F.; Sahraoui, B. A Switchable NLO Organic-Inorganic Compound Based on Conformationally Chiral Disulfide Molecules and Bi(III)I_5 Iodobismuthate Networks. *Adv. Mater.* **2008**, *20*, 1013−1017.
(29) Bi, W.; Louvain, N.; Mercier, N.; Luc, J.; Sahraoui, B. Type structure, which is composed of organic diammonium, triiodide and hexaiodobismuthate, varies according to different structures of incorporated cations. *CrystEngComm* **2007**, *9*, 298−303.
(30) Mercier, N.; Barres, A.-L.; Giffard, M.; Rau, I.; Kajzar, F.; Sahraoui, B. Conglomerate-to-True-Racemate Reversible Solid-State Transition in Crystals of an Organic Disulfide-Based Iodoplumbate. *Angew. Chem., Int. Ed.* **2006**, *45*, 2100−2103.
(31) Deng, W.-F.; Li, Y.-X.; Zhao, Y.-X.; Hu, J.-S.; Yao, Z.-S.; Tao, J. Inversion of Molecular Chirality Associated with Ferroelectric Switching in a High-Temperature Two-Dimensional Perovskite Ferroelectric. *J. Am. Chem. Soc.* **2023**, *145*, 5545−5552.
(32) Zhang, R.; Cai, W.; Bi, T.; Zarifi, N.; Terpstra, T.; Zhang, C.; Verdeny, Z. V.; Zurek, E.; Deemyad, S. Effects of Nonhydrostatic Stress on Structural and Optoelectronic Properties of Methylammonium Lead Bromide Perovskite. *J. Phys. Chem. Lett.* **2017**, *8*, 3457−3465.
(33) Wang, Y.; Sun, X.; Shao, T.; Zhao, D.; Zhang, L.; Li, Y.; Dong, Q.; Liu, C.; Wang, K.; Xiao, G.; Zou, B. Band-Gap Narrowing and Electric Transport Regulation of Hybrid Perovskites via Pressure Engineering. *Inorg. Chem.* **2024**, *63*, 11431−11437.
(34) Sobczak, S.; Fidelli, A. M.; Do, J.-L.; Demopoulos, G. P.; Moores, A.; Friščić, T.; Katrusiak, A. High-pressure Observation of Elusive Iodoplumbic Acid in Different Hydronium-Hydrate Solid Forms. *Inorg. Chem. Front.* **2024**, *11*, 735−744.
(35) Mączka, M.; Sobczak, S.; Ratajczyk, P.; Leite, F. F.; Paraguassu, W.; Dybała, F.; Herman, A. P.; Kudrawiec, R.; Katrusiak, A. Pressure-Driven Phase Transition in Two-Dimensional Perovskite MHy$_2$PbBr$_4$. *Chem. Mater.* **2022**, *34*, 7867−7877.
(36) Zhang, Y.; Li, Z.-G.; Song, H.; Yang, T.-Y.; Wu, X.; Cai, W.; Zhang, J.; Li, W.; Bu, X.-H. Linear Regulation of Red Emission in an Organic−Inorganic Manganese Bromide via Pressure. *Chem. Mater.* **2024**, *36*, 3435−3443.
(37) Mao, L.; Ke, W.; Pedesseau, L.; Wu, Y.; Katan, C.; Even, J.; Wasielewski, M. R.; Stoumpos, C. C.; Kanatzidis, M. G. Hybrid Dion−Jacobson 2D Lead Iodide Perovskites. *J. Am. Chem. Soc.* **2018**, *140*, 3775−3783.
(38) Szafrański, M.; Katrusiak, A. Mechanism of Pressure-Induced Phase Transitions, Amorphization, and Absorption-Edge Shift in Photovoltaic Methylammonium Lead Iodide. *J. Phys. Chem. Lett.* **2016**, *7*, 3458−3466.
(39) Aizu, K. Possible Species of "Ferroelastic" Crystals and of Simultaneously Ferroelectric and Ferroelastic Crystals. *J. Phys. Soc. Jpn.* **1969**, *27*, 387−396.
(40) Jiang, D.; Jiang, X.; Zhang, X.; Li, C.; Liu, K.; Ma, Y.; Cheng, H.-M.; Pei, T.; Wen, T.; Lin, Z.; et al. Second-Harmonic-Generation Switching via Pressure-Suppressed Dynamical Disorder. *J. Am. Chem. Soc.* **2024**, *146*, 23508−23516.

https://doi.org/10.1021/acs.chemmater.5c00335
Chem. Mater. 2025, 37, 2953−2963

(41) Sobczak, S.; Nowok, A.; Zaręba, J. K.; Roszak, K.; Półrolniczak, A.; Szeremeta, A. Z.; Dziuk, B.; Dybała, F.; Pawlus, S.; Kudrawiec, R.; et al. Expanding the Horizons of the Thermodynamic Landscape and Optoelectronic Properties of Soft 2D Hybrid Perovskites MHy_2PbX_4. *J. Mater. Chem. A* **2024**, *12*, 16803−16814.
(42) Zhang, D.; Fu, B.; He, W.; Li, H.; Liu, F.; Wang, L.; Liu, H.; Zhou, L.; Cai, W. Pressure-Induced Shape and Color Changes and Mechanical-Stimulation-Driven Reverse Transition in a One-Dimensional Hybrid Halide. *Nat. Commun.* **2024**, *15*, No. 6678.
(43) Xu, B.; Li, Y.; Hong, P.; Zhang, P.; Han, J.; Xiao, Z.; Quan, Z. Pressure-Controlled Free Exciton and Self-Trapped Exciton Emission in Quasi-One-Dimensional Hybrid Lead Bromides. *Nat. Commun.* **2024**, *15*, No. 7403.
(44) Krishnamurthy, S.; Kour, P.; Katre, A.; Gosavi, S.; Chakraborty, S.; Ogale, S. Cystamine-Configured Lead Halide Based 2D Hybrid Molecular Crystals: Synthesis and Photoluminescence Systematics. *APL Mater.* **2018**, *6*, No. 114204.
(45) Hooft, R. W. W.; Straver, L. H.; Spek, A. L. Determination of Absolute Structure using Bayesian Statistics on Bijvoet Differences. *J. Appl. Crystallogr.* **2008**, *41*, 96−103.
(46) Robinson, K.; Gibbs, G. V.; Ribbe, P. H. Quadratic Elongation: A Quantitative Measure of Distortion in Coordination Polyhedra. *Science* **1971**, *172*, 567−570.
(47) Fu, C.; Dai, C.; Du, B.; Li, P.; Lei, L.; Hu, F.; Jiang, Z. Raman Spectroscopic Study of Orthorhombic L-Cysteine under Pressure up to 20.2 GPa. *J. Mol. Struct.* **2018**, *1171*, 196−201.
(48) Su, Y.; Hessou, E. P.; Colombo, E.; Belletti, G.; Moussadik, A.; Lucas, I. T.; Frochot, V.; Daudon, M.; Rouzière, S.; Bazin, D.; et al. Crystalline Structures of L-Cysteine and L-Cystine: a Combined Theoretical and Experimental Characterization. *Amino Acids* **2022**, *54*, 1123−1133.
(49) Hernández, B.; Pflüger, F.; López-Tobar, E.; Kruglik, S. G.; Garcia-Ramos, J. V.; Sanchez-Cortes, S.; Ghomi, M. Disulfide Linkage Raman Markers: a Reconsideration Attempt. *J. Raman Spectrosc.* **2014**, *45*, 657−664.
(50) Zhang, L.; Li, S.; Sun, H.; Fang, Y.; Wang, Y.; Wang, K.; Jiang, H.; Sui, L.; Wu, G.; Yuan, K.; et al. Manipulating Lone-Pair-Driven Luminescence in 0D Tin Halides by Pressure-Tuned Stereochemical Activity from Static to Dynamic. *Angew. Chem., Int. Ed.* **2023**, *62*, No. e202311912.
(51) Fang, Y.; Shao, T.; Zhang, L.; Sui, L.; Wu, G.; Yuan, K.; Wang, K.; Zou, B. Harvesting High-Quality White-Light Emitting and Remarkable Emission Enhancement in One-Dimensional Halide Perovskites upon Compression. *JACS Au* **2021**, *1*, 459−466.
(52) Zhang, L.; Wang, K.; Lin, Y.; Zou, B. Pressure Effects on the Electronic and Optical Properties in Low-Dimensional Metal Halide Perovskites. *J. Phys. Chem. Lett.* **2020**, *11*, 4693−4701.
(53) Yin, W.-J.; Yang, J.-H.; Kang, J.; Yan, Y.; Wei, S.-H. Halide Perovskite Materials for Solar Cells: a Theoretical Review. *J. Mater. Chem. A* **2015**, *3*, 8926−8942.
(54) Fu, Y. Stabilization of Metastable Halide Perovskite Lattices in the 2D Limit. *Adv. Mater.* **2022**, *34*, No. 2108556.
(55) Walsh, A.; Payne, D. J.; Egdell, R. G.; Watson, G. W. Stereochemistry of Post-Transition Metal Oxides: Revision of the Classical Lone Pair Model. *Chem. Soc. Rev.* **2011**, *40*, 4455−4463.
(56) Liu, S.; Sun, S.; Gan, C. K.; del Águila, A. G.; Fang, Y.; Xing, J.; Do, T. T. H.; White, T. J.; Li, H.; Huang, W.; Xiong, Q. Manipulating Efficient Light Emission in Two-Dimensional Perovskite Crystals by Pressure-Induced Anisotropic Deformation. *Sci. Adv.* **2019**, *5*, No. eaav9445.
(57) Pyykko, P.; Desclaux, J. P. Relativity and the Periodic System of Elements. *Acc. Chem. Res.* **1979**, *12*, 276−281.
(58) Laurita, G.; Seshadri, R. Chemistry, Structure, and Function of Lone Pairs in Extended Solids. *Acc. Chem. Res.* **2022**, *55*, 1004−1014.
(59) Mao, H. K.; Xu, J.; Bell, P. M. Calibration of the Ruby Pressure Gauge to 800 kbar under Quasi-Hydrostatic Conditions. *J. Geophys. Res.* **1986**, *91*, 4673−4676.
(60) Staško, D.; Prchal, J.; Klicpera, M.; Aoki, S.; Murata, K. Pressure Media for High Pressure Experiments, Daphne Oil 7000 Series. *High Pressure Res.* **2020**, *40*, 525−536.
(61) Sheldrick, G. M. A Short History of SHELX. *Acta Crystallogr., Sect. A:Found. Crystallogr.* **2008**, *64*, 112−122.
(62) Angel, R. J.; Alvaro, M.; Gonzalez-Platas, J. EosFit7c and a Fortran module (library) for equation of state calculations. *Z. Kristallogr. - Cryst. Mater.* **2014**, *229*, 405−419.
(63) Kresse, G.; Joubert, D. From Ultrasoft Pseudopotentials to the Projector Augmented-Wave Method. *Phys. Rev. B* **1999**, *59*, No. 1758.
(64) Blöchl, P. E. Projector Augmented-Wave Method. *Phys. Rev. B* **1994**, *50*, No. 17953.
(65) Kresse, G.; Furthmüller, J. Efficient Iterative Schemes for ab initio Total-Energy Calculations Using A Plane-Wave Basis Set. *Phys. Rev. B* **1996**, *54*, 11169−11186.
(66) Kresse, G.; Furthmüller, J. Efficiency of ab-initio Total Energy Calculations for Metals and Semiconductors using a Plane-Wave Basis Set. *Comput. Mater. Sci.* **1996**, *6*, 15−50.
(67) Dronskowski, R.; Bloechl, P. E. Crystal Orbital Hamilton Populations (COHP): Energy-Resolved Visualization of Chemical Bonding in Solids based on Density-Functional Calculations. *J. Phys. Chem. A* **1993**, *97*, 8617−8624.
(68) Deringer, V. L.; Tchougréeff, A. L.; Dronskowski, R. Crystal Orbital Hamilton Population (COHP) Analysis As Projected from Plane-Wave Basis Sets. *J. Phys. Chem. A* **2011**, *115*, 5461−5466.
(69) Maintz, S.; Deringer, V. L.; Tchougréeff, A. L.; Dronskowski, R. Analytic Projection from Plane-Wave and PAW Wave Functions and Application to Chemical-Bonding Analysis in Solids. *J. Comput. Chem.* **2013**, *34*, 2557−2567.
(70) Perdew, J. P.; Burke, K.; Ernzerhof, M. Generalized Gradient Approximation Made Simple. *Phys. Rev. Lett.* **1996**, *77*, No. 3865.
(71) Nelson, R.; Ertural, C.; George, J.; Deringer, V. L.; Hautier, G.; Dronskowski, R. LOBSTER: Local Orbital Projections, Atomic Charges, and Chemical-Bonding Analysis from Projector-Augmented-Wave-Based Density-Functional Theory. *J. Comput. Chem.* **2020**, *41*, 1931−1940.

https://doi.org/10.1021/acs.chemmater.5c00335
Chem. Mater. 2025, 37, 2953−2963